analytical chemistry

ACS AuthorChoice

Article

pubs.acs.org/ac

Terms of Use

Separation of *Escherichia coli* Bacteria from Peripheral Blood Mononuclear Cells Using Standing Surface Acoustic Waves

Ye Ai,*[,†] Claire K. Sanders,[‡] and Babetta L. Marrone*[,‡]

[†]Pillar of Engineering Product Development, Singapore University of Technology and Design, Singapore 138682, Singapore

[‡]Bioscience Division, Los Alamos National Laboratory, Los Alamos, New Mexico 87545, United States

Supporting Information

ABSTRACT: A microfluidic device was developed to separate heterogeneous particle or cell mixtures in a continuous flow using acoustophoresis. In this device, two identical surface acoustic waves (SAWs) generated by interdigital transducers (IDTs) propagated toward a microchannel, which accordingly built up a standing surface acoustic wave (SSAW) field across the channel. A numerical model, coupling a piezoelectric effect in the solid substrate and acoustic pressure in the fluid, was developed to provide a better understanding of SSAW-based particle manipulation. It was found that the pressure nodes across the channel were individual planes perpendicular to the solid substrate. In the separation experiments, two side sheath flows hydrodynamically focused the injected particle or cell mixtures into a very narrow stream along the centerline. Particles flowing through the SSAW field experienced an acoustic radiation force that highly depends on the particle properties. As a result, dissimilar particles or cells were laterally attracted toward the pressure nodes at different magnitudes, and were eventually switched to different outlets. Two types of fluorescent microspheres with different sizes were successfully separated using the developed device. In addition, *Escherichia coli* bacteria premixed in peripheral blood mononuclear cells (PBMCs) were also efficiently isolated using the SSAW-base separation technique. Flow cytometric analysis on the collected samples found that the purity of separated *E. coli* bacteria was 95.65%.

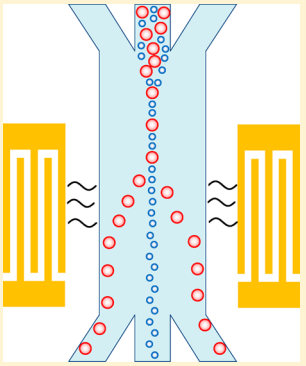

Biological samples generally consist of highly heterogeneous cell populations. As a result, an effective separation of specific cell types is usually required prior to further biomedical analysis. Most biological cells carry a size on the order of a few to tens of micrometers, which renders microfluidics an ideal platform for efficient cell separation. To date, several techniques including dielectrophoresis, magnetophoresis, flow fractionation, and inertia flow have been implemented to separate synthetic particles or biological cells in microfluidic devices, as comprehensively reviewed by Lenshof and Laurell.[1]

Acoustophoresis, referring to the migration of particles subjected to acoustic waves, has recently emerged as a new noninvasive technique for particle separation in microfluidics. In such a scheme, piezoelectric transducers are introduced to generate a standing acoustic wave field. A particle exposed to the acoustic field is subjected to an acoustic radiation force that is highly dependent on its physical properties, such as size, density, and compressibility. Therefore, acoustophoresis can selectively manipulate particles or biological cells based on their physical properties, which is more flexible than existing label-free manipulation techniques. As a result, heterogeneous cell mixtures could be separated based on different motion responses arising from the acoustic radiation effect. In addition, acoustophoresis has no or minor negative impact on the viability and functionality of biological cells,[2] required in many cell analysis applications. Most earlier acoustic-based microfluidic devices were constructed by attaching a bulk acoustic transducer onto a silicon microchannel. Incident acoustic waves, together with the reflection from the channel wall, can form a standing acoustic wave field across the channel. Separation of particles or biological cells with different physical properties has been successfully demonstrated using bulk standing acoustic waves.[3−10] Since the development of soft lithography,[11] soft polymer materials, such as polydimethylsiloxane (PDMS), have been widely adopted in the fabrication of microfluidic devices. However, most of these polymer materials have a quite poor acoustic reflection property, which make them incompatible with bulk acoustic transducers. In addition, bulk acoustic transducers cannot be easily miniaturized and integrated with other microstructures.

Recently, surface acoustic wave (SAW) devices have gained increased attention due to their low power consumption, flexible design, easy miniaturization, and integration into microfluidic devices. A standing surface acoustic wave (SSAW) field can be generated across a microchannel by radiating two identical SAWs toward the channel. Shi et al. observed a particle focusing phenomenon subjected to a SSAW field,[12] which was later used for two-dimensional (2D) particle patterning.[13,14] Separation of dissimilar synthetic particles in a continuous flow using SSAW has been successfully demonstrated.[15,16] Moreover, isolation of platelets from a blood sample has been implemented using the same technique.[17] All

Received: June 13, 2013
Accepted: August 23, 2013
Published: August 23, 2013

   dx.doi.org/10.1021/ac4017715 | *Anal. Chem.* 2013, 85, 9126−9134

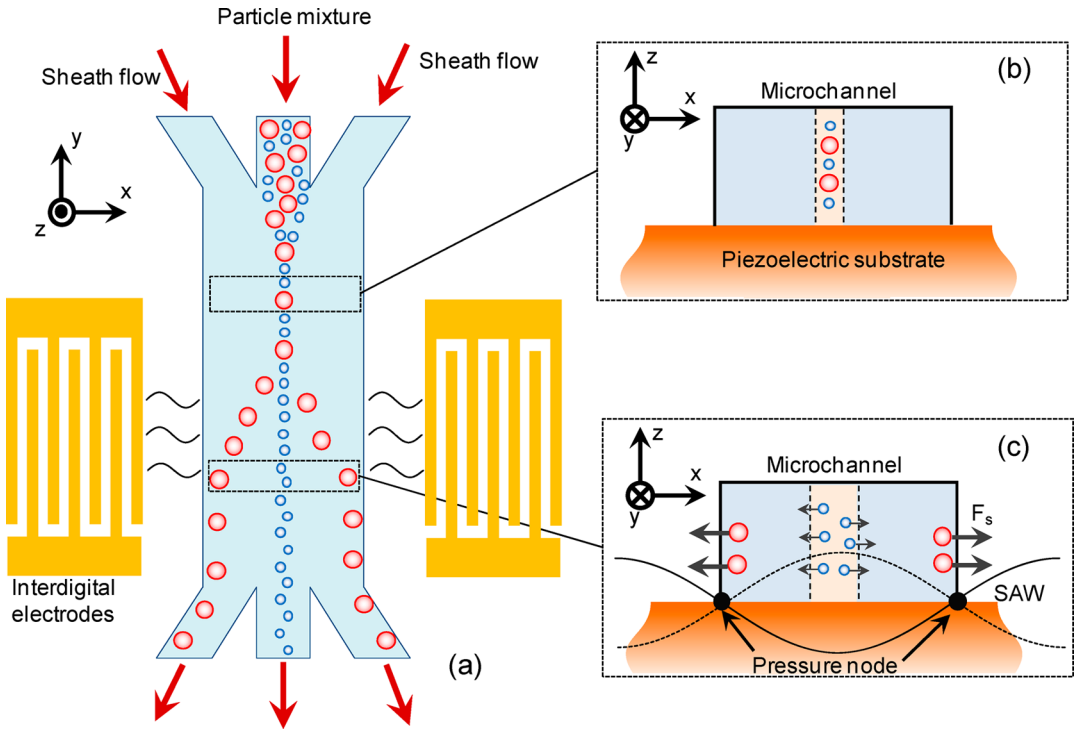

Figure 1. (a) Schematic illustration of the microfluidic device and separation mechanism using a SSAW field. A mixture solution with two differently sized particles is focused to the centerline of the channel by two faster side sheath flows. A SSAW field is generated by two IDTs on both sides of the channel. Dissimilar particles experience different lateral movement in the SSAW field arising from the size-dependent acoustic radiation force. As a result, the two particles are shifted to different outlets. (b) Cross-section of the hydrodynamic focusing before the SSAW field. (c) Cross-section of the SSAW-induced particle separation. Pressure nodes are located at the two sidewalls where the two particles are attracted.

the aforementioned particle separations were primarily based on different lateral movements induced by size-dependent acoustic radiation effects. As the acoustic radiation force acting on the particle also depends on its density, the application of SSAW on density-based particle separation has also been recently demonstrated.[18] Most recently, SSAW was utilized to sort individual droplets dispersed in an oil phase.[19,20] In addition to the application of SSAW for particle manipulation, a single traveling SAW has also been widely used for mixing, pumping, and transport of fluids or droplets in microfluidics.[21−27] It is very obvious that SAW has become a promising and versatile technique for noninvasive manipulation of fluids and particles in microfluidics.

In this article, we presented a SSAW-based microfluidic device for efficient separation of synthetic particles and biological cells. Most previous SSAW-based devices were designed to have one single pressure node in the middle of the microchannel. This design requires a very tight alignment of SAW devices with the microchannel to maintain an efficient separation. In our design, the pressure nodes of the SSAW field were located near the two sidewalls of the microchannel. When the width of the microchannel is smaller than a half acoustic wavelength, the alignment of SAW devices with the microchannel is not very critical, which accordingly reduces the complexity of fabrication. A numerical model was developed to simulate the acoustic pressure field across the channel generated by the SSAW field, which provided an insight into the SSAW-based particle manipulation. Two different particle mixtures were used in the separation demonstration to validate the developed device: fluorescent synthetic microspheres of different sizes and human peripheral blood mononuclear cells (PBMCs) mixed with *Escherichia coli* bacteria. The ability to separate bacteria from blood cells would enable rapid diagnosis of bloodstream related infections.[28] Human immune function could also be evaluated by measuring the proliferation or other changes in PBMCs stimulated with *E. coli* or other bacteria.[29,30] The efficiency of the *E. coli*/PBMCs separation was quantitatively evaluated by traditional flow cytometric analysis.

WORKING PRINCIPLE AND THEORY

Acoustic Radiation and Working Principle. Figure 1 shows the schematic illustration of the developed microfluidic device and the working principle of size-based particle separation using a SSAW field. The SSAW generator is basically a pair of interdigital transducers (IDTs) patterned on a piezoelectric substrate. A microchannel is located between the two IDTs to form the microfluidic device. When an ac signal is applied to the IDTs, two series of identical SAWs propagate toward the microchannel in opposite directions. Constructive interference of the two SAWs gives rise to a SSAW field across the channel. Particles through the SSAW field are subjected to a time-averaged acoustic radiation force, given as[31]

$$\langle F_S \rangle = -\nabla\left\{\frac{V_p}{4\rho_f c_f^2}\left[2\left(1-\frac{1}{\beta\gamma^2}\right)\langle p^2\rangle - \frac{2\beta-2}{2\beta+1}\frac{3}{k^2}\langle|\nabla p|^2\rangle\right]\right\} \quad (1)$$

In the above, V_p is the volume of the particle, ρ_f is the density of the fluid medium, c_f is the speed of sound in the fluid medium, $\beta = \rho_p/\rho_f$ is the density ratio, and $\gamma = c_p/c_f$ is the speed of sound

dx.doi.org/10.1021/ac4017715 | *Anal. Chem.* 2013, 85, 9126−9134

ratio. The subscripts "p" and "f" denote, respectively, the material parameters for solid particle and fluid medium. p is the pressure generated by the acoustic wave, $k = \omega/c_f$ is the wavenumber with ω denoting the angular frequency. Considering a one-dimensional model with x denoting the distance from the pressure node, the pressure can be expressed as

$$p(x, t) = p_0 \cos(kx) \cos(\omega t) \tag{2}$$

where p_0 is the pressure magnitude. Substituting eq 2 into eq 1, we can get

$$\langle F_S \rangle = -\nabla\left\{\frac{V_p}{4\rho_f {c_f}^2}\left[2\left(1 - \frac{1}{\beta\gamma^2}\right){p_0}^2 \cos^2(kx)\langle\cos^2(\omega t)\rangle - \frac{2\beta - 2}{2\beta + 1}\frac{3}{k^2}k^2{p_0}^2 \sin^2(kx)\langle\cos^2(\omega t)\rangle\right]\right\} \tag{3}$$

The time average term, $\langle\cos^2(\omega t)\rangle = 1/2$, can further simplify eq 3 as[32]

$$\langle F_S \rangle = 2k\frac{V_p {p_0}^2}{8\rho_f {c_f}^2}\varphi(\beta, \gamma) \sin(2kx) \tag{4}$$

where

$$\varphi(\beta, \gamma) = \frac{5\beta - 2}{2\beta + 1} - \frac{1}{\beta\gamma^2} \tag{5}$$

is the acoustic contrast factor. When $\varphi(\beta,\gamma) > 0$, the acoustic radiation force pushes particles to the pressure node where the pressure change is always zero. On the contrary, particles are attracted to the antipressure node when $\varphi(\beta,\gamma) < 0$. In general, most solid particles and biological cells suspended in aqueous solutions have a positive acoustic contrast factor and are thus attracted to the pressure node.[8] The resonant frequency of the generated SSAW mainly depends on the distance between two adjacent electrode fingers of the IDTs. In this device, the wavelength of the resonant SSAW is approximately twice the channel width, and the pressure nodes are located at the two sidewalls of the channel, as shown in Figure 1. The entrance of the device has three inlets with the particle mixture solution in the middle and the sheath flow at the two sides. The faster sheath flow hydrodynamically focuses the particle mixture into a very narrow stream along the centerline of the channel, as shown in Figure 1. When particles enter the SSAW field, the size-dependent acoustic radiation force starts to attract particles into the pressure node. Larger particles laterally move to the pressure node at the sidewalls faster than smaller particles, resulting in the size-based particle separation. Therefore, larger particles are switched to the side outlets and are accordingly separated from smaller particles flowing into the middle outlet, as shown in Figure 1.

Numerical Modeling. A finite element method (FEM) based numerical model (COMSOL Multiphysics 4.3, www.comsol.com) was developed to study the acoustic-piezoelectric interaction problem. As the SSAW is uniform in the longitudinal direction of the channel, we simply considered a 2D modeling of the device cross-section in a frequency analysis. Therefore, the acoustic-piezoelectric interaction module at frequency domain was selected to perform the modeling of the developed SSAW-based device. A PDMS layer was located on the top of a piezoelectric substrate, and a tiny fluid layer was sealed between them. The propagation of SAW in a piezoelectric substrate is governed by the Maxwell's equations for electric field and the stress−strain equations for mechanical motion. The linear piezoelectric constitutive equations are given as

$$\mathbf{T} = \mathbf{C}_E\cdot\mathbf{S} - \mathbf{e}^{tr}\cdot\mathbf{E} \tag{6}$$

$$\mathbf{D} = \mathbf{e}\cdot\mathbf{S} + \boldsymbol{\varepsilon}\cdot\mathbf{E} \tag{7}$$

where $\mathbf{T}$ is the mechanical stress vector, $\mathbf{C}_E$ is the elasticity matrix, $\mathbf{S}$ is the strain vector, $\mathbf{e}$ is the piezoelectric stress matrix, $\mathbf{E}$ is the electric field vector, $\mathbf{D}$ is the electric displacement vector, and $\boldsymbol{\varepsilon}$ is the dielectric matrix. The superscript "tr" represents the transpose of the matrix. The acoustic pressure field in the fluid and PDMS domains is governed by the well-known Helmholtz equation,

$$\frac{1}{\rho_i'}\nabla^2 p - \frac{\omega^2 p}{\rho_i {c_i}^2} = 0 \tag{8}$$

where

$$\rho_i' = \frac{\rho_i {c_i}^2}{\omega^2}\left(\frac{\omega}{c_i} - j\ln(10)\frac{\alpha_i}{20}\right)^2 \tag{9}$$

In the above, ρ_i, c_i, and α_i are the density, speed of sound, and acoustic attenuation coefficient in the corresponding domain, $j = (-1)^{1/2}$ is the imaginary unit. The acoustic velocity is given by

$$v_i = -\frac{j}{\omega\rho_i'}\nabla p \tag{10}$$

For the electric field in the piezoelectric substrate, a sinusoidal ac signal with a peak-to-peak magnitude of 10 V was applied to the interdigital electrodes on the piezoelectric substrate. The other boundaries of the piezoelectric substrate were assumed zero charge surfaces. For the elastic mechanical motion arising from the piezoelectric effect, the surface with interdigital electrodes, excluding boundaries in contact with the fluid and PDMS domains, was set to free, referring to no force loads or constraints. Because of the interaction between the elastic mechanical motion and acoustic pressure field, a force load was applied on the boundaries in contact with the fluid and PDMS domains,

$$\mathbf{T}\cdot\mathbf{n} = -p\mathbf{n} \tag{11}$$

where $\mathbf{n}$ is the unite normal vector of the applied boundaries. Zero normal displacement was applied on all the other boundaries. The harmonic vibration of the piezoelectric substrate propagated acoustic waves into the fluid and PDMS at the interface, which is mathematically described by an acceleration boundary condition

$$n\cdot\left(-\frac{\nabla p}{\rho_i'}\right) = a_n \tag{12}$$

Strictly speaking, the standing acoustic wave field in the fluid across the channel was actually generated by the SAWs radiated into the fluid from the piezoelectric substrate. The outer surface of the PDMS domain was specified as a sound hard boundary

$$n\cdot\left(-\frac{\nabla p}{\rho_i'}\right) = 0. \tag{13}$$

dx.doi.org/10.1021/ac4017715 | Anal. Chem. 2013, 85, 9126−9134

Acoustic pressure and velocity were continuous across the interface between the fluid and PDMS. Simulations with different mesh sizes were implemented to ensure that numerical results were converged and mesh-independent. A coarse mesh with a size of 20 μm was generated near the bottom of the piezoelectric substrate, and a fine mesh with a size of 3 μm was employed in the microchannel to accurately capture the pressure nodes of the SSAW field.

DEVICE FABRICATION AND EXPERIMENTAL DETAILS

Chip Fabrication. The PDMS channel in the device was fabricated using a standard soft lithography technique.[11] Briefly, a 25 μm thick negative photoresist (SU-8 25, MicroChem Corp., Newton, MA) was first spin-coated on a clean glass slide, followed by a two-step soft bake (65 °C for 3 min and 95 °C for 7 min). The photoresist covered by a 20 000 dpi mask with a channel pattern was then exposed to 365 nm ultraviolet light with an energy density of 150 mJ/cm^2 (Figure 2a), followed by another two-step hard bake (65 °C for 1 min and 95 °C for 3 min). Subsequently, a master mold was obtained by developing the photoresist in a commercial SU-8 developer solution for 4 min (Figure 2b). Degassed PDMS mixture (Sylgard184 Silicone Elastomer Kit, Dow Corning Corp., Freeland, MI) of prepolymer and curing agent at a ratio of 10:1 by weight were poured over the master and cured at 65 °C for 4 h (Figure 2c). The fully cured PDMS was peeled off from the master mold. Inlet and outlet holes were created using a small drill bit for external tubing interconnection. The IDTs for SSAW generation were fabricated on a 128° rotated Y-cut X-propagating lithium niobate ($LiNbO_3$) piezoelectric substrate using a lift-off technique. Basically, the $LiNbO_3$ substrate was first spin-coated with a 1.25 μm thick positive photoresist (AZ 5214E-IR, Capitol Scientific, Dallas, TX), followed by a soft bake (100 °C for 60 s). The mask-covered photoresist was patterned by exposing to the ultraviolet light with an energy density of 70 mJ/cm^2, followed by a 35 s development in AZ 300 MIF developer solution (Figure 2d). A double metallic layer (Cr/Au, 5 nm/80 nm) was then deposited onto the developed $LiNbO_3$ substrate by an electron beam evaporator (Figure 2e). Subsequently, the $LiNbO_3$ substrate was sonicated in acetone for half an hour to remove photoresist and undesired Cr/Au layer on its top (Figure 2f). The previously obtained PDMS substrate and the patterned $LiNbO_3$ substrate were loaded into an oxygen plasma cleaner (Harrick Plasma Inc., Ithaca, NY) for surface activation (Figure 2g). Later, the two substrates were well aligned under a microscope with the assistance of markers on both substrates and were eventually brought into contact to form permanent bonding (Figure 2h).

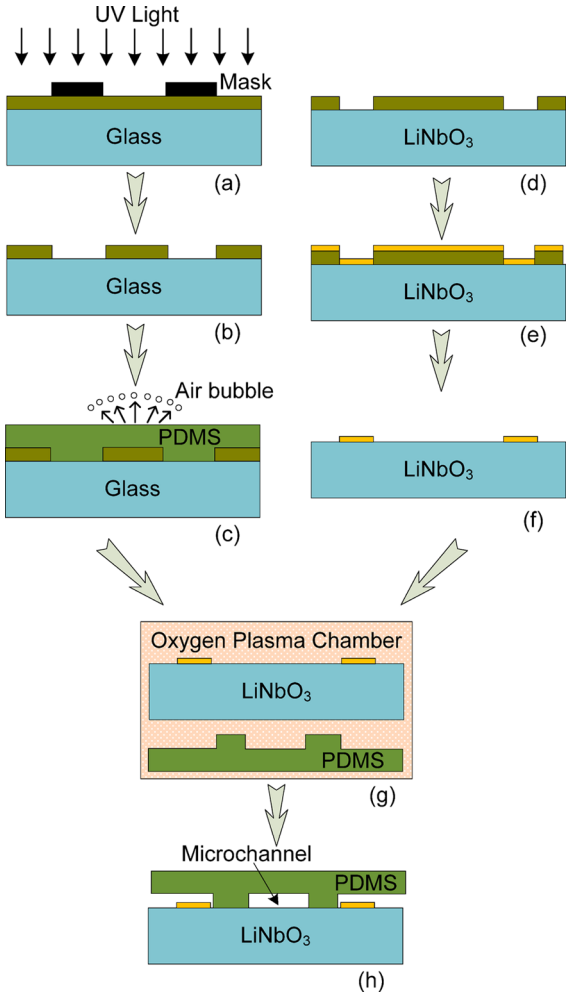

Figure 2. Fabrication procedure of the microfluidic device: (a–c) fabrication of the PDMS microchannel, (d–f) patterning of IDTs on the $LiNbO_3$ substrate, and (g,h) surface activation and bonding of the two layers to form the device.

Experimental Setup. Figure 3 shows the image of the final microfluidic device. The width and height of the main channel

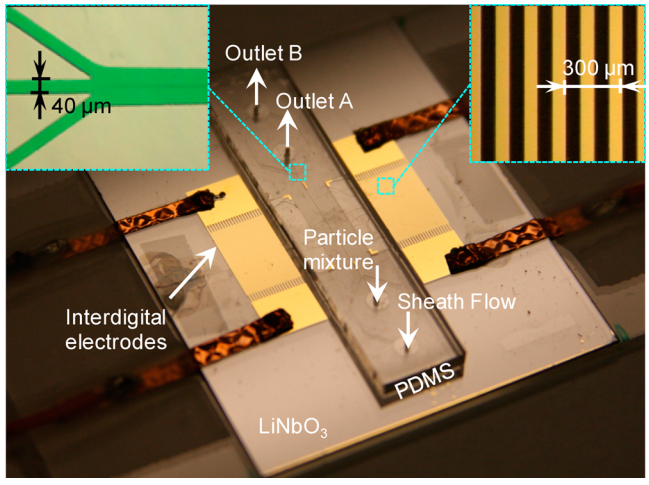

Figure 3. Photograph of the fabricated microfluidic device for particle separation. The upper-left inset is the zoomed-in view of the three-outlet junction. The upper-right inset is the zoomed-in view of the IDT.

are 120 and 25 μm, respectively. The lengths of the main channel and IDTs are 15 mm and 9 mm, respectively. Each IDT has 20 electrode finger pairs with 300 μm finger pitch and 75 μm finger width, corresponding to a SAW wavelength of λ = 300 μm. The channel width is slightly smaller than the half wavelength, which aims to provide a reasonable tolerance for the alignment prior to the permanent bonding. Therefore, a tight alignment of IDTs with the microchannel is not critical to achieve an efficient separation. The speed of sound in $LiNbO_3$ substrate is approximately 3900 m/s, leading to a resonant frequency around 13 MHz. In practice, the best resonant frequency of the fabricated IDTs was found to be 13.0168 MHz

dx.doi.org/10.1021/ac4017715 | Anal. Chem. 2013, 85, 9126–9134

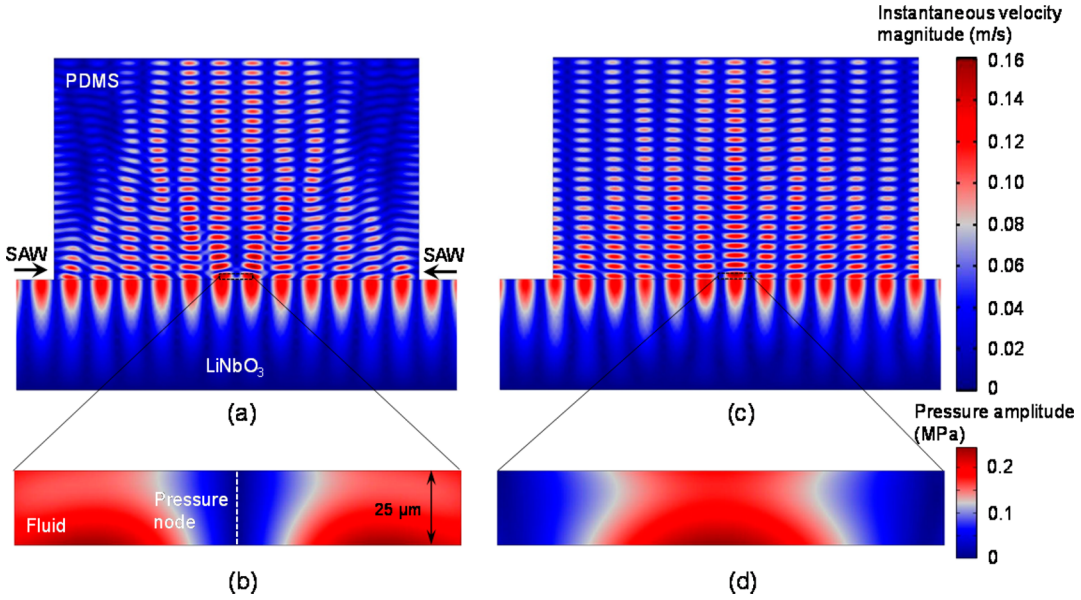

Figure 4. Numerical results of a SSAW field on the cross-section when the fluid is located in the midpoint between the two IDTs (a) and when the fluid is shifted 1/4 wavelength to the right (c). Corresponding pressure field in the fluid with a pressure node along the centerline (b) and two pressure nodes at the sidewalls (d).

by an impedance analysis. A sinusoidal ac signal at the resonant frequency was generated by a signal generator (Tektronix, Beaverton, OR) and then amplified by a power amplifier (OPHIR RF, Los Angeles, CA). The IDTs were excited by the amplified ac signal to generate a SSAW field across the channel. The device was loaded on the stage of a fluorescence microscope (Zeiss Axioskop Microscope) to conduct the separation experiments. Particle mixtures (cell mixtures) and DI water (1× phosphate buffered saline solution) were, respectively, injected into the device through the inlets labeled "particle mixture" and "sheath flow" using syringe pumps (New Era Pump Systems Inc., Farmingdale, NY). In order to avoid particle or cell adhesion to the channel wall, all the solutions were mixed with 0.5% surfactant of Pluronic F68 (Invitrogen Corp., Carlsbad, CA). Particle motion and separation were captured and recorded at 30 frames per second by a Sony camcorder installed on the microscope. Fluorescence filters were manually switched to visualize a specific excitation and emission light of fluorescent particles or stained cells. The recorded videos were later processed by a free image processing program, ImageJ (National Institutes of Health, http://rsbweb.nih.gov/ij/).

Sample Preparation. Two different particle mixtures were used in the separation experiments. The first mixture included two types of fluorescent synthetic microspheres (Particle I, 1.2 μm in diameter, green emission; Particle II, 5.86 μm in diameter, red emission, both from Polysciences Inc., Warrington, PA). Both particles were diluted to a concentration of 2×10^7 particles/mL. The second sample was a mixture of purified human PBMCs (Bioreclamation LLC, Hicksville, NY) and *E. coli* bacteria. PBMCs were washed and then fixed for 15 min using 2% formaldehyde in phosphate buffered saline (PBS) solution. Cells were stained with 1 μg/mL Hoechst 33342 (Calbiochem, Billerica, MA) for 10 min, spun down and resuspended in PBS. The average size of PBMCs is approximately 7.23 μm in diameter. Thermostable green protein (TGP, ECGP123 variant) expressing BL21 *E. coli* bacteria were induced with isopropyl β-D-1-thiogalactopyranoside (IPTG) for 4 h at 30 °C and then grown on kan agar overnight at 37 °C.[33] Later, the bacteria were resuspended in PBS and mixed with the PBMC solution. *E. coli* bacteria are typically rod-shaped with a diameter of 0.5 μm and a length of 2 μm, which has a similar volume as a sphere with a diameter of 1.1 μm. The concentration of both cells is approximately 3×10^6 particles/mL. Separation purity of the cell mixture was determined by a flow cytometric analysis (LSR II, Becton Dickenson, San Jose, CA). Pure samples were used to calibrate the settings and also exclude the debris from the cytometric results. A combination of relative size based on light scatter and whether the cells were positive for Hoechst or TGP-10 was used to evaluate purity.

RESULTS AND DISCUSSION

Simulation of SSAW Field. To theoretically verify the design of the SSAW-based particle separation, we first applied the FEM model to simulate the SAW propagation and acoustic pressure field generated on the cross-section of the fabricated device. A frequency analysis from 12.2 to 13.2 MHz was performed to find the resonant frequency, which was around 12.98 MHz and agreed well with the practical value. The attenuation coefficients of water and PDMS at 13 MHz are 36.67 dB/m[34] and 8224 dB/m,[35] respectively. Figure 4a shows the numerical result of the acoustic velocity field on the cross-section of the device, in which the fluid and PDMS are located in the midpoint between two IDTs. Two identical SAWs propagate from both sides toward the fluid and PDMS. When the SAW first encounters the PDMS, it partially radiates into the PDMS at a Rayleigh angle, $\theta_R = \arcsin(c_{PDMS}/c_L)$, where c_{PDMS} and c_L are, respectively, the speed of sound in the PDMS and $LiNbO_3$. As the two individual SAWs travel further and meet each other, the constructive interference of the two SAWs forms a SSAW field in the $LiNbO_3$ and also across the fluid and PDMS layers, as shown in Figure 4a. The distance between two adjacent peaks is half of the SSAW wavelength. It is calculated from the numerical modeling that the SSAW wavelength in the $LiNbO_3$ is about 300 μm, equal to the designed IDT pitch. The

dx.doi.org/10.1021/ac4017715 | *Anal. Chem.* 2013, 85, 9126−9134

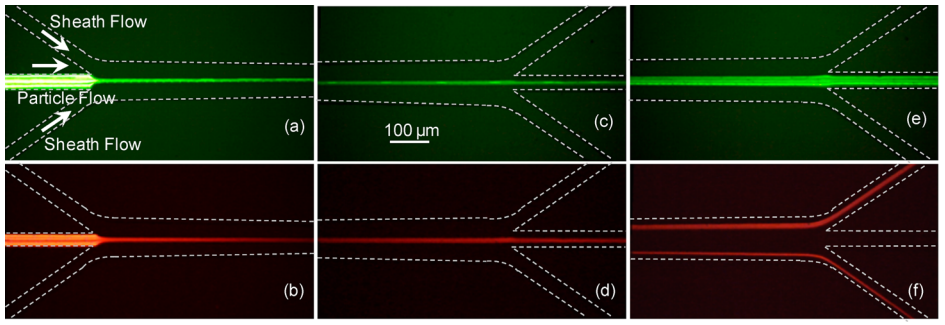

Figure 5. Captured fluorescence images at the inlet junction (a,b) and outlet junction (c–f) in one single experiment by tuning the power applied on the IDTs. No SSAW field was applied in parts c and d, while a SSAW field with a power of 23.8 dBm was applied in parts e and f. Flow rates of the particle flow and a single side sheath flow were, respectively, 0.2 μL/min and 0.8 μL/min. Green and red emission lights represent the 1.2 μm Particle I and the 5.86 μm Particle II, respectively. Each image was obtained by superimposing a series of images captured at the same location. Dashed lines represent the boundary of the microchannel.

SSAW in the PDMS layer along the vertical direction has a shorter wavelength because the speed of sound in the PDMS is lower than that in the $LiNbO_3$. Because of the attenuation effect, the SSAW strength gradually decreases as it is located further from the interface between PDMS and $LiNbO_3$. Figure 4b shows the resulting acoustic pressure field inside the fluid. The pressure node with a zero magnitude is a single plane perpendicular to the $LiNbO_3$ substrate, located in the horizontal center of the channel. As a result, suspended particles with a positive acoustic contrast factor are attracted to the middle of the channel, referring to the acoustic focusing effect.[12] In Figure 4c, the fluid and PDMS are shifted 75 μm toward the IDT on the right-hand side. Similarly, a SSAW field is generated over the entire cross-section of the device. However, the pressure node is shifted to the two sidewalls of the channel, as shown in Figure 4d. Therefore, the location of the pressure node across the channel can be precisely controlled during the alignment process prior to the permanent bonding. To verify the location of the pressure node in the fabricated device, a highly concentrated 5.86 μm Particle II was injected into the channel and eventually became stationary with a random distribution. A SSAW field was subsequently turned on with a power of 23.8 dBm (1 dBm = 10 log(U), where U is the input power applied on the IDTs in the unit of mW). Movie file 1 in the Supporting Information shows that all the particles were quickly attracted and accumulated at the two sidewalls of the channel once the SSAW field was turned on. This observation confirmed that the pressure node in this device is located at the sidewalls. Some particles, initially located at the same distance from one of the sidewalls, moved toward the sidewall at different speeds. This phenomenon may be attributed to the nonuniform acoustic pressure field at different heights of the channel, which was verified by the numerical results shown in Figure 4b,d.

Separation of Synthetic Microspheres. Next, the separation of the first mixture (1.2 μm Particle I and 5.86 μm Particle II) was demonstrated using the fabricated device. The flow rates of the particle mixture and the sheath flow were 0.2 μL/min and 1.6 μL/min, respectively. The sheath flow was later evenly split into two side streams at the inlet junction (Figure 5a); therefore, the flow rate of each individual side sheath flow was 0.8 μL/min. As the inlet junction is away from the SSAW field, a pure hydrodynamic focusing of both particles to the centerline of the channel was observed (Figure 5a,b). When the SSAW field was turned off, both particles kept flowing near the centerline along the entire channel due to the nature of a laminar flow. Therefore, both particles flowed into the middle outlet (Figure 5c,d). The motion of both particles at the outlet junction without a SSAW field can be seen from movie file 2 in the Supporting Information. Later, a SSAW field with a power of 23.8 dBm was turned on. When the particle mixture entered the SSAW field, the acoustic radiation force acting on the 5.86 μm Particle II was much greater than that acting on the 1.2 μm Particle I. Therefore, the larger Particle II was pulled out of the particle mixture, laterally moving toward the pressure node at the sidewalls. The acoustic radiation force was maximized at the antipressure node and gradually decreased to zero when approaching the pressure node. As a result, the lateral movement stopped at the pressure node, and Particle II exactly followed the sheath flow thereafter. The acoustic radiation force acting on the smaller Particle I was insufficient to pull it out of the middle stream before leaving the SSAW field. Thus, Particle I remained near the centerline at the outlet junction and flowed into the middle outlet (Figure 5e). Particle II, however, was switched to the side outlets (Figure 5f), indicating a successful separation. The separation of the two particles using a SSAW field can be seen from movie file 3 in the Supporting Information.

Figure 6 shows the particle trajectories in the middle region of the SSAW field with different input powers. When the SSAW field was turned off, the two particles both remained near the centerline (Figure 6a,b), exactly as they were at the inlet junction. When a SSAW field with a power of 19.3 dBm was turned on, Particle I stayed near the centerline due to a weak acoustic radiation force and an insufficient SSAW exposure time (Figure 6c). In contrast, Particle II started to laterally shift toward the two sidewalls (Figure 6d). When the power of SSAW field was further increased to 25.3 dBm, the stream width of Particle I became larger as a result of a minor lateral movement (Figure 6e). Meanwhile, Particle II was further laterally shifted near the sidewalls because of an increased acoustic radiation force (Figure 6f). An efficient SSAW-based separation relies on a sufficient difference in lateral movements of dissimilar particles. In order to achieve the SSAW-based separation at high flow rates, one can increase the input power or maintain a sufficient SSAW exposure time by extending the SSAW field.

Separation of *E. coli* and PBMCs. Finally, we used this device to separate *E. coli* bacteria from PBMC samples. Both cells were found to move toward the pressure node when exposed to a SSAW field, indicating a positive acoustic contrast. We increased the flow rates of both cell mixture and sheath

dx.doi.org/10.1021/ac4017715 | *Anal. Chem.* 2013, 85, 9126–9134

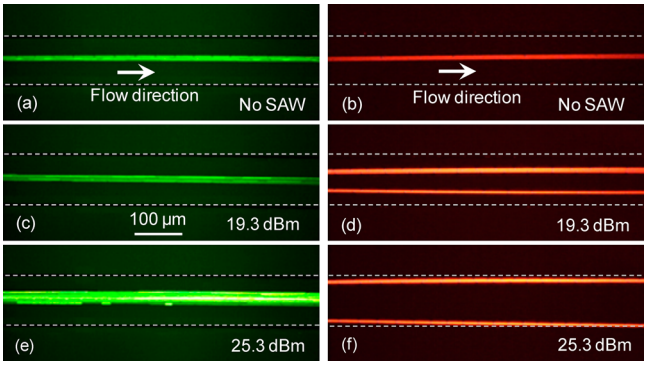

Figure 6. Captured fluorescence images at the middle region of the channel in one single experiment by tuning the power applied on the IDTs: (a,b) no SSAW field, (c,d) a SSAW field with a power of 19.3 dBm, (e,f) A SSAW field with a power of 25.3 dBm. Green and red emission lights represent the 1.2 μm Particle I and the 5.86 μm Particle II, respectively. Each image was obtained by superimposing a series of images captured at the same location. Dashed lines represent the boundary of the microchannel.

flow to test the throughput of the developed device. Hence, the power applied on the IDTs was increased to maintain a sufficient lateral movement for PBMCs. The optimum acoustic power was determined by observing the cell separation at the outlet junction under the microscope. The fluorescence of stained *E. coli* bacteria was not very bright, and when the flow rate of the cell mixture was too high, it was quite difficult to observe the trajectory of *E. coli* bacteria. Therefore, the visibility of the cell separation process limits the throughput of the developed device. To clearly visualize the separation process, the maximum flow rate of the cell mixture should not exceed 0.5 μL/min, which was used in the separation of *E. coli* and PBMCs. Accordingly, the flow rate of the sheath flow was adjusted to 4 μL/min to maintain a highly focused middle stream before entering the SSAW field. A SSAW field with a power of 26.7 dBm was turned on for about 4 h to separate the two cells in a continuous flow. The separated *E. coli* bacteria and PBMCs were, respectively, collected from the outlets labeled "Outlet A" and "Outlet B", as shown in Figure 3. The premixture and collected samples were analyzed in a flow cytometer to quantify the respective cell contents. The ratio of each cell type was defined as the number of corresponding cells detected through the flow cytometer to the total number of counted cells. The cell populations were plotted in terms of forward scatter (FSC) and side scatter (SSC) to show the cell content in each sample. Figure 7a confirms that the premixture mainly consisted of *E. coli* and PBMCs with very little debris. The ratios of *E. coli* and PBMCs in the premixture were, respectively, 46.23% and 53.06% (Figure 7d), as they were intended to mix at a similar cell concentration. After flowing

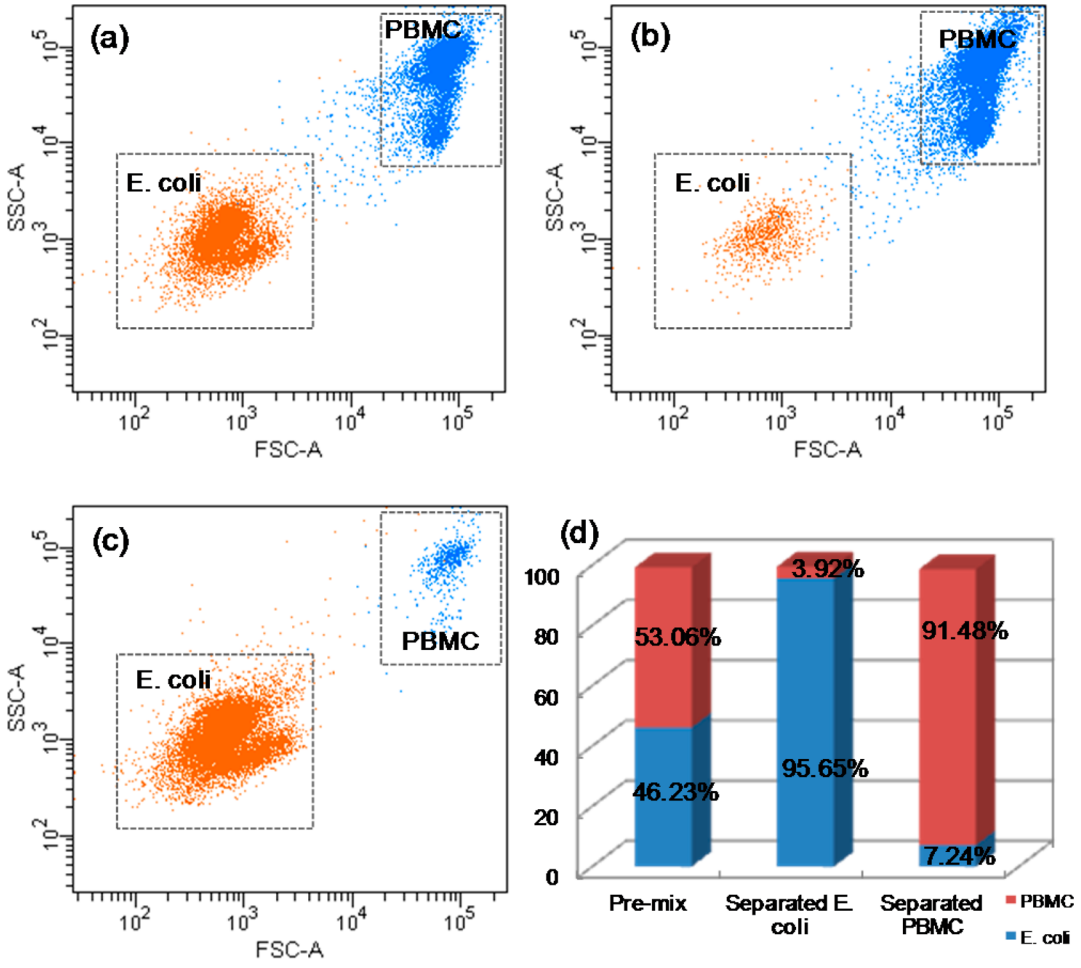

Figure 7. Flow cytometric scatter plots (forward scatter versus side scatter) of the premixture (a), separated PBMC sample (b), and separated *E. coli* sample (c). (d) Quantitative cell content in each sample.

dx.doi.org/10.1021/ac4017715 | *Anal. Chem.* 2013, 85, 9126−9134

through the SSAW field, *E. coli* bacteria were successfully extracted from the premixture, as shown in Figures 7b and 7c. The ratios of *E. coli* and PBMCs in the samples collected from the outlets labeled "Outlet A" and "Outlet B" were, respectively, 95.65% and 91.48% (Figure 7d). The difference in density and compressibility of *E. coli* and PBMCs could result in the different acoustic contrast factors and eventually affect the acoustic radiation forces acting on the cells. However, we found that the cell size remains the key factor influencing the separation of *E. coli* from PBMCs. These results demonstrated that the developed device could effectively separate synthetic particles or biological cells based on their sizes using a SSAW field.

CONCLUSIONS

We have demonstrated the efficient separation of dissimilar particles or cells in a continuous flow using a SSAW field with a resonant frequency near 13 MHz. The configuration of two pressure nodes near the sidewalls of the channel narrower than a half acoustic wavelength reduces the requirement for the alignment of IDTs with the channel. A FEM model was developed to simulate the acoustic pressure field generated by the SAWs radiated into the fluid, which is of great help to understand the SSAW-based particle manipulation. In this device with a channel height of 25 μm, the pressure nodes across the channel were individual planes perpendicular to the $LiNbO_3$ substrate. The location of the pressure node across the channel could be adjusted by shifting the location of the channel with respect to the IDTs on both sides. Particles and biological cells used in this study had positive acoustic contrast factors, which moved them toward the pressure node as a result of the acoustic radiation effect. The 5.86 μm particles were successfully separated from the 1.2 μm particles based on different lateral movements toward the pressure nodes located at the two sidewalls. The separation efficiency and throughput of a SSAW-based device can be adjusted by tuning the applied acoustic power and flow rates of the sheath flow and particle mixture. The throughput of the developed device was limited by the visibility of the cell separation process, which could be overcome by integrating sensors capable of size measurement in all the outlets. Separation of *E. coli* bacteria from premixed PBMCs with a purity of 95.65% indicates that this technique could be further developed to diagnose bacteria-induced bloodstream infections and assist the evaluation of immune responses of PBMCs. Conclusively, the SSAW-based separation technique is a promising approach for the isolation of specific cell types from heterogeneous biological samples for a variety of applications.

ASSOCIATED CONTENT

Supporting Information

Movie files 1–3. This material is available free of charge via the Internet at http://pubs.acs.org.

AUTHOR INFORMATION

Corresponding Authors

*E-mail: aiye@sutd.edu.sg.
*E-mail: blm@lanl.gov.

Notes

The authors declare no competing financial interest.

ACKNOWLEDGMENTS

This work was supported by the National Center for Research Resources and the National Institute of General Medical Sciences of the National Institutes of Health (Grant P41 RR01315) through the National Flow Cytometry Resource (B.L.M.), by a Laboratory Directed Research and Development award (20130239ER) from Los Alamos National Laboratory (B.L.M.) and, in part, by the International Design Center (Grant IDG11300101) from Singapore University of Technology and Design–Massachusetts Institute of Technology Alliance (Y.A.). This work was performed, in part, at the Center for Integrated Nanotechnologies, a U.S. Department of Energy, Office of Basic Energy Sciences user facility, and we gratefully acknowledge Jon Kevin Baldwin for the assistance of Cr/Au deposition. We also would like to thank Patricia S. Langan for providing TGP expressing *E. coli*.

REFERENCES

(1) Lenshof, A.; Laurell, T. *Chem. Soc. Rev.* **2010**, *39* (3), 1203–1217.
(2) Burguillos, M. A.; Magnusson, C.; Nordin, M.; Lenshof, A.; Augustsson, P.; Hansson, M. J.; Elmér, E.; Lilja, H.; Brundin, P.; Laurell, T.; Deierborg, T. *PLoS ONE* **2013**, *8* (5), e64233.
(3) Petersson, F.; Nilsson, A.; Holm, C.; Jonsson, H.; Laurell, T. *Analyst* **2004**, *129* (10), 938–943.
(4) Petersson, F.; Nilsson, A.; Holm, C.; Jonsson, H.; Laurell, T. *Lab Chip* **2005**, *5* (1), 20–22.
(5) Petersson, F.; Nilsson, A.; Jonsson, H.; Laurell, T. *Anal. Chem.* **2005**, *77* (5), 1216–1221.
(6) Petersson, F.; Åberg, L.; Swärd-Nilsson, A. M.; Laurell, T. *Anal. Chem.* **2007**, *79* (14), 5117–5123.
(7) Jung, B.; Fisher, K.; Ness, K. D.; Rose, K. A.; Mariella, R. P. *Anal. Chem.* **2008**, *80* (22), 8447–8452.
(8) Liu, Y.; Lim, K.-M. *Lab Chip* **2011**, *11* (18), 3167–3173.
(9) Yang, A. H. J.; Soh, H. T. *Anal. Chem.* **2012**, *84* (24), 10756–10762.
(10) Cushing, K. W.; Piyasena, M. E.; Carroll, N. J.; Maestas, G. C.; López, B. A.; Edwards, B. S.; Graves, S. W.; López, G. P. *Anal. Chem.* **2013**, *85* (4), 2208–2215.
(11) Xia, Y. N.; Whitesides, G. M. *Annu. Rev. Mater. Sci.* **1998**, *28*, 153–184.
(12) Shi, J. J.; Mao, X. L.; Ahmed, D.; Colletti, A.; Huang, T. J. *Lab Chip* **2008**, *8* (2), 221–223.
(13) Shi, J. J.; Ahmed, D.; Mao, X.; Lin, S. C. S.; Lawit, A.; Huang, T. J. *Lab Chip* **2009**, *9* (20), 2890–2895.
(14) Ding, X.; Shi, J.; Lin, S.-C. S.; Yazdi, S.; Kiraly, B.; Huang, T. J. *Lab Chip* **2012**, *12* (14), 2491–2497.
(15) Shi, J. J.; Huang, H.; Stratton, Z.; Huang, Y. P.; Huang, T. J. *Lab Chip* **2009**, *9* (23), 3354–3359.
(16) Nam, J.; Lee, Y.; Shin, S. *Microfluid. Nanofluid.* **2011**, *11* (3), 317–326.
(17) Nam, J.; Lim, H.; Kim, D.; Shin, S. *Lab Chip* **2011**, *11* (19), 3361–3364.
(18) Jo, M. C.; Guldiken, R. *Sens. Actuators, A: Phys.* **2012**, *187* (0), 22–28.
(19) Nam, J.; Lim, H.; Kim, C.; Kang, J. Y.; Shin, S. *Biomicrofluidics* **2012**, *6* (2), 024120.
(20) Li, S.; Ding, X.; Guo, F.; Chen, Y.; Lapsley, M. I.; Lin, S.-C. S.; Wang, L.; McCoy, J. P.; Cameron, C. E.; Huang, T. J. *Anal. Chem.* **2013**, *85*, 5468–5474.
(21) Wixforth, A.; Strobl, C.; Gauer, C.; Toegl, A.; Scriba, J.; von Guttenberg, Z. *Anal. Bioanal. Chem.* **2004**, *379* (7–8), 982–991.
(22) Shilton, R.; Tan, M. K.; Yeo, L. Y.; Friend, J. R. *J. Appl. Phys.* **2008**, *104* (1), 014910.
(23) Renaudin, A.; Sozanski, J.-P.; Verbeke, B.; Zhang, V.; Tabourier, P.; Druon, C. *Sens. Actuators, B* **2009**, *138* (1), 374–382.
(24) Brunet, P.; Baudoin, M.; Matar, O. B.; Zoueshtiagh, F. *Phys. Rev. E* **2010**, *81* (3), 036315.

(25) Ai, Y.; Marrone, B. L. *Microfluid. Nanofluid.* **2012**, *13* (5), 715−722.
(26) Masini, L.; Cecchini, M.; Girardo, S.; Cingolani, R.; Pisignano, D.; Beltram, F. *Lab Chip* **2010**, *10* (15), 1997−2000.
(27) Trung-Dung, L.; Vinh-Nguyen, P.; Nam-Trung, N. *Microfluid. Nanofluid.* **2011**, *10* (3), 619−625.
(28) Mach, A. J.; Adeyiga, O. B.; Di Carlo, D. *Lab Chip* **2013**, *13* (6), 1011−1026.
(29) Kew, S.; Banerjee, T.; Minihane, A. M.; Finnegan, Y. E.; Williams, C. M.; Calder, P. C. *Am. J. Clin. Nutr.* **2003**, *77* (5), 1278−1286.
(30) Komura, T.; Sakai, Y.; Honda, M.; Takamura, T.; Matsushima, K.; Kaneko, S. *Diabetes* **2010**, *59* (3), 634−643.
(31) Gorkov, L. P. *Sov. Phys. Doklady* **1962**, *6*, 773.
(32) Yosioka, K.; Kawasima, Y. *Acustica* **1955**, *5*, 167−173.
(33) Kiss, C.; Temirov, J.; Chasteen, L.; Waldo, G. S.; Bradbury, A. R. M. *Protein Eng., Des. Sel.* **2009**, *22* (5), 313−323.
(34) Mordfin, L., *Handbook of Reference Data for Nondestructive Testing*; ASTM International: West Conshohocken, PA, 2002.
(35) Tsou, J. K.; Liu, J.; Barakat, A. I.; Insana, M. F. *Ultrasound Med. Biol.* **2008**, *34* (6), 963−972.